Two-dimensional strain rate imaging study using a polarization camera and birefringent aqueous cellulose nanocrystal suspensions

Journal Article

Author(s):
Lane, Connor; Baumann, Frédéric; Rode, David; Rösgen, Thomas

RESEARCH ARTICLE

Two-dimensional strain rate imaging study using a polarization camera and birefringent aqueous cellulose nanocrystal suspensions

Connor Lane[1] · Frédéric Baumann[1] · David Rode[1] · Thomas Rösgen[1]

Abstract

The birefringence response of aqueous cellulose nanocrystal (CNC) suspensions in a two-dimensional laminar flow is measured and studied. The suspensions have CNC concentrations of 1.0 wt% (weight percentage) and 1.2 wt%. Cellulose nanocrystals are optically anisotropic rod-like particles that align when subjected to local velocity gradients, whereas at rest, they remain randomly orientated by Brownian motion. The alignment causes birefringence, a phenomenon also known as flow-induced birefringence. We study the flow through an additively manufactured flow channel and measure the amount of birefringence as well as the position of the refractive index axes by using polarizers and a polarization camera. With the help of reference data published in a previous study (Lane, Rode, et al., 2022a), strain rates are derived from the birefringence measurements and compared with numerical simulations. Two flow situations are studied, a plane Poiseuille flow and the flow around a cosine-shaped constriction. The experimentally derived shear rates for the plane Poiseuille flow are consistent with theoretical and computational results. The derived strain rates for the flow around the cosine-shaped constriction show an unexpected asymmetric profile, with the strain rates in the contraction zone being larger than in the expansion zone. The averaged orientation of the CNCs in the flow is linked to the position of the refractive index axes. In the contraction zone, the CNCs tend to align parallel to the flow, whereas in the expansion zone, the CNCs tend to align perpendicular to the flow. The results of this study are discussed in the context of previous, similar studies. The asymmetric strain rate profile around the cosine-shaped constriction is thought to originate from history effects, and the alignment of the CNCs is influenced by extensional rates.

1 Introduction

Birefringent fluids are composed of optically anisotropic particles or macromolecules (Merzkirch 2001). At rest, Brownian motion randomly orientates these particles, and the birefringent fluid is optically isotropic. Local velocity gradients align the particles and, as a result, the fluid becomes optically anisotropic. This phenomenon is also referred to as flow-induced birefringence and can be used to visualize and study fluid flows (Hu et al. 2009; Pih 1980; Rankin et al. 1989; C. Sun & Huang 2016) as well as to assess particle alignment and rheological properties (Fuller 1995; Janeschitz-Kriegl 1983). The amount of birefringence is expressed by the difference Δn between the two main refractive indices n_1 and n_2. In this study, we define

n_1 as the refractive index associated with the fast axis, i.e., $n_1 < n_2$. Generally, Δn is a function of the strain rate $\dot{\epsilon}$, where increasing $\dot{\epsilon}$ increases Δn. Various experimental methods have been applied to determine $\Delta n(\dot{\epsilon})$ and therefore to characterize a birefringent fluid (Calabrese et al. 2021; Lane et al. 2021a; Mykhaylyk et al. 2016). Note that we use the expression strain rate instead of shear rate in this study to be more general. If u and v are the velocity components in x- and y- direction, respectively, and subscripts x and y indicate the directional derivatives, we define the strain rate magnitude of the two-dimensional flow as

$$\dot{\epsilon} = \sqrt{2u_x^2 + 2v_y^2 + \left(u_y + v_x\right)^2} = \sqrt{4u_x^2 + \left(u_y + v_x\right)^2}. \quad (1)$$

The 2D incompressibility condition $u_x = -v_y$ was inserted above. For a pure shearing flow with a velocity gradient in the y-direction only, we get $\dot{\epsilon} = \dot{\gamma} = u_y$. A derivation of Eq. (1) as well as its application in the context of flow birefringence can be found in the study by Peebles and Liu (1965). The fluid flow simulation software used in Sect. 2.5,

✉ Connor Lane
clane@ethz.ch

1 Institute of Fluid Dynamics, ETH Zürich, Sonneggstrasse 3, 8092 Zurich, Switzerland

Ansys Fluent (Ansys 2022), defines the strain rate magnitude as $\dot{\epsilon} = \sqrt{2 \cdot \boldsymbol{E} : \boldsymbol{E}}$, with $\boldsymbol{E}$ being the strain rate tensor. This definition equally leads to Eq. (1) for a two-dimensional, incompressible flow.

Many flow birefringence studies use an industrial dye called Milling Yellow (Peebles et al. 1964; Schneider 2013; Sun et al. 1999). Other fluids such as solutions of tobacco mosaic virus have also been employed (Hu et al. 2009). Cellulose nanocrystals (CNCs) are rod-like particles, and the refractive index of their longitudinal axis is larger than the refractive index of the semi-axes (Frka-Petesic et al. 2015). A recent study reports birefringence measurements of aqueous CNC suspensions and suggests their use in flow birefringence studies (Lane, Rode, et al. 2022a). Measuring shear and strain rates with the help of birefringence seems advantageous, as the technique is noninvasive. Notably, the similar photoelastic technique has recently been used to measure and visualize complex stress fields in soft materials (Mitchell et al. 2023; Miyazaki et al. 2021; Rapet et al. 2019; Yokoyama et al. 2023).

In this study, the magnitude of the birefringence response Δn as well as the position of the slow axis n_2 of an aqueous CNC suspension in a two-dimensional flow is measured with the help of a polarization camera. The orientation of the slow axis n_2 is related to the predominant direction of the longitudinal axis of the nanorods and therefore, describes the averaged orientation of the CNCs in the fluid flow. Strain rates are derived with the help of reference data previously published (Lane, Rode, et al. 2022a, tbl. 2) and are compared to simulation results.

Parts of this study have been presented and discussed previously (Lane, Baumann, et al. 2022) and detailed in a thesis (Lane 2022). The present paper collects these findings, adds information on the particle size distribution and the particle orientation, and discusses the findings in the context of the available literature.

2 Material and methods

2.1 Aqueous cellulose nanocrystal suspension

Two aqueous CNC suspensions with CNC concentrations of 1.0 wt% (weight percentage) and 1.2 wt% were prepared by dispersing CelluForce NCC® powder (CelluForce Inc., celluforce.com) into distilled water. The suspensions were prepared one week prior to the experiments so that the nanocrystals could disperse homogeneously. Lane et al. (2022a) used similar suspensions, which are thought to be above the dilute regime and particle interactions must therefore be taken into account.

Transmission electron microscopy (TEM) was used to estimate the size distribution of the CNCs. For this, the CNCs were dispersed in purified water at a concentration of 2 mg/ml. A droplet of 4 μl was placed on a negatively glow-discharged carbon coated copper grid and imaged using TEM (ThermoFischer Scientific Tecnai F20; magnification of 29kX and 62kX, leading to pixel sizes of 3.55Å and 1.7 Å, respectively). Lengths and diameters of 887 CNCs were analyzed using the FiJi image processing package. An exemplary image and the results are shown in Fig. 1. The means of length, diameter, and aspect ratio are 108.3 nm (standard deviation (SD) 43.5 nm), 7.3 nm (SD 2.7 nm), and 15.9 (SD 6.7), respectively. These values are comparable to the results (mean length, mean diameter) of Jakubek et al. (2018) (TEM: 87 nm, 7.4 nm; atomic force microscopy: 77 nm, 3.5 nm) and Bertsch et al. (2018) (atomic force microscopy: 79 nm, 4.8 nm), who analyzed CNCs from the same supplier.
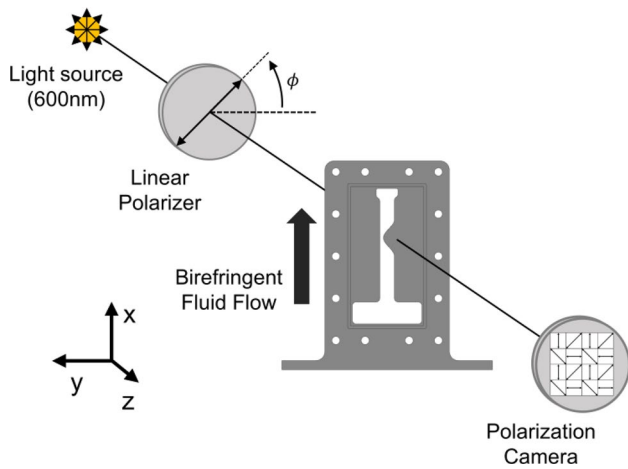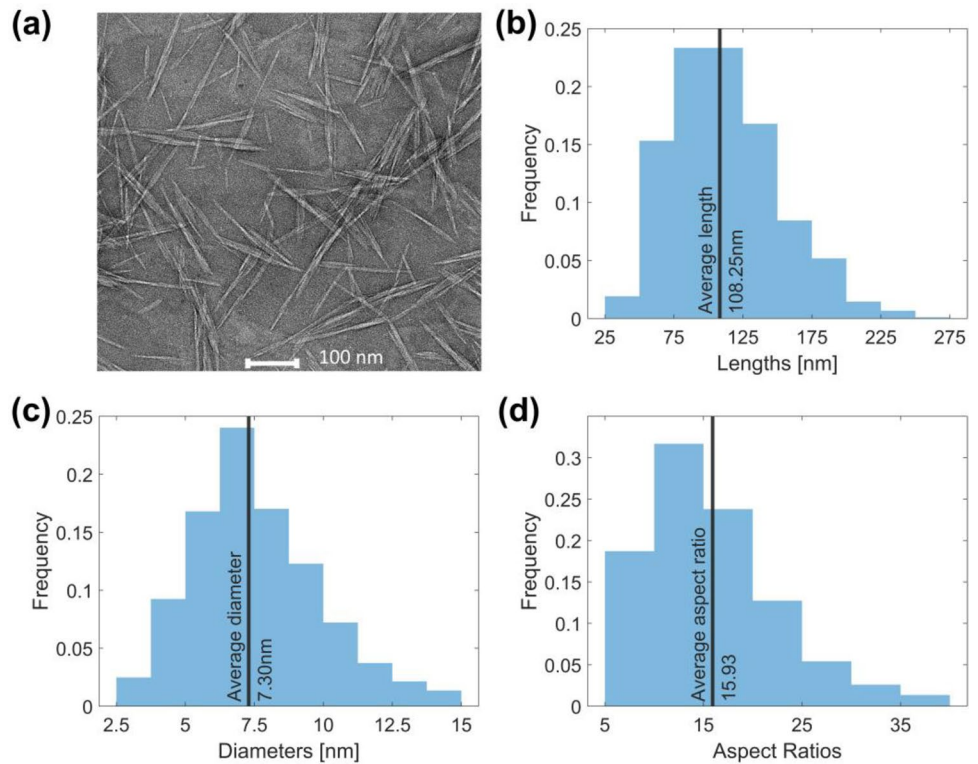
2.2 Experimental set-up

The experimental set-up is shown in Fig. 2. It consists of a light source (halogen bulb; 150W EKE), a color filter (600 nm bandpass filter; 600FS10-50 from Andover Corporation, HBW 10 nm), a rotatable linear polarizer (Techspec Glass polarizer 50.8 m; Edmund Optics Inc #66–183; extinction ratio 10,000:1; continuous manual rotation mount Thorlabs Part RSP2/M), a fluid flow cell, and a polarization camera. To measure the absolute position of the slow refractive index axis (which corresponds to the preferential direction in which the CNCs are aligned), a right-handed circular polarizer (Plastic Circular Polarizer, Edmund Optics Inc #88–102; polarization Efficiency > 99.9%) was used instead of the linear polarizer. The polarization camera (Phoenix PHX050S-P, Lucid Vision Labs (2022)) is equipped with a high resolution telecentric lens (TC4MHR036-C, Opto Engineering; working f/#: 16). Polarization measurement errors from the polarization camera are estimated to be below 3% due to the sufficiently large f-number (Lane et al. 2022b).

The flow channel was prepared using an additive manufacturing technique (3D Printer: Form3 Formlabs; Material: Clear Resin). The channel dimensions can be seen in Fig. 3a. The cosine-shaped constriction is described as

$$y = 3mm + 3mm \cdot \cos\left[\frac{x}{10mm} \cdot \pi\right] \text{for} -10mm \leq x \leq 10mm. \tag{2}$$

The flow direction is upwards. The main 3D printed part is shown in Fig. 3b. The front and back surfaces were milled to create plane surfaces. Additionally, a sealing groove was machined into each surface. Two glass plates flush with the surfaces sealed the flow channel. Note that the lens was focused on the front glass (the glass closest to the lens). Focusing the lens on the middle or on the rear glass led to strong distortions. The flow inside the channel was driven by

Fig. 1 Size distribution of 887 analyzed CNCs using TEM: (**a**) Exemplary TEM image taken with a magnification of 62kX. (**b**) Lengths. (**c**) Diameters. (**d**) Aspect ratios


Fig. 2 Experimental set-up. Light is sent through a rotatable linear polarizer and the birefringent fluid flow. A polarization camera captures the optical response

a computer-controlled micro-stepping syringe pump (Cavro XLP 6000, Tecan).

2.3 Two-dimensional birefringence measurement technique

We apply the measurement technique described in (Lane et al. 2021b) to measure the two-dimensional flow birefringence response Δn. The linear polarizer is rotated to nine
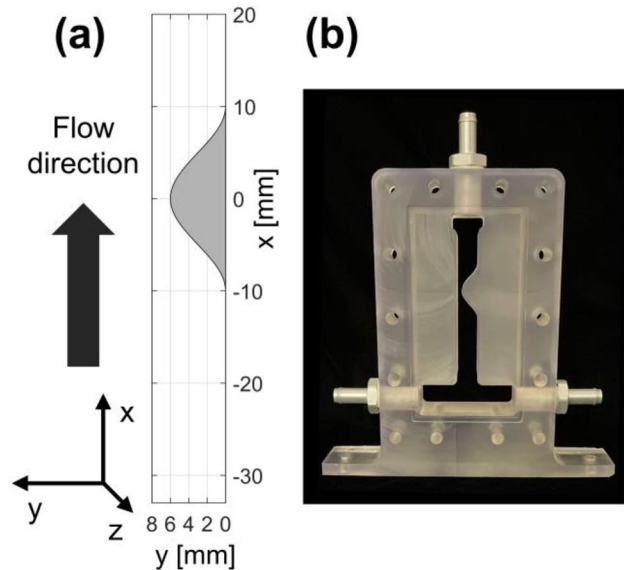
Fig. 3 Studied flow channel. (**a**) Dimensions in x and y direction. The depth in the z-direction is 25 mm. (**b**) 3D printed part

different positions: $\phi = 0° + 20° \cdot N$ with $N = 0, 1, 2, \dots, 8$. At each position, the light transmitted through the birefringent flow is captured by the polarization camera. The polarization camera measures the state of linear polarization. From the nine measurements, the relative phase difference δ is calculated, from which the birefringence is determined:

$$\Delta n = \frac{\lambda}{2\pi \cdot L} \cdot \delta. \tag{3}$$

Here, $L=25$ mm is the path length and $\lambda = 600 nm$ the wavelength. Equation (3) requires that the optical properties are constant along the path length. Even though the actual flow is three-dimensional, we assume an essentially two-dimensional flow and therefore expect Eq. (3) to be a valid approximation. This aspect is discussed more deeply in Sect. 3.1.

The measurement technique referred to has a measurement range for the phase difference of π radian (half the wavelength). We limit ourselves to this measurement range (corresponding to a maximum of $\Delta n = 1.2 \cdot 10^{-5}$), because in this interval the measured (relative) phase differences are the actual phase differences and Eq. (3) is directly applicable. To increase the measurement range of the phase difference above π radian, multiple wavelengths can be applied (Ajovalasit et al. 2015).

In order to measure the position θ_{slow} of the slow refractive index axis (equivalent to the averaged rod orientation), we use circular instead of linear polarized light. Applying Stokes parameters and Mueller matrices similar to the approach presented by Onuma and Otani (2014), the following relation can be derived for right-handed circular polarized light passing through a linear birefringent sample that induces a phase difference δ and where the fast refractive index axis is orientated at the angle ϕ_{fast},

$$S_1 = -I_0 \cdot \sin 2\phi_{fast} \cdot \sin\delta, \tag{4.1}$$

$$S_2 = I_0 \cdot \cos 2\phi_{fast} \cdot \sin\delta \tag{4.2}$$

$$S_3 = I_0 \cdot \cos\delta. \tag{4.3}$$

We derive the formulas by means of the fast axis, as the fast axis is commonly used to describe optical elements. Here, S_1, S_2 and S_3 are the second, third, and fourth Stokes parameters (the first one is $S_0 = I_0$) and I_0 is the intensity of the polarized light. The reference coordinate system is arbitrary. However, it is important that ϕ_{fast} and S_1 and S_2 refer to the same one. Equations (4.1) and (4.2) result in

$$\phi_{fast} = \frac{1}{2}\operatorname{atan2}(-S_1, S_2). \tag{5}$$

Note that Eq. (5) is only valid for $0 \le \delta \le \pi$, because for $\delta > \pi$ the signs have to be changed due to $\sin(\delta + \pi) = -\sin(\delta)$, giving $\phi_{fast} = 1/2 \cdot \operatorname{atan2}(S_1, -S_2)$. The direction of the slow refractive index axis is given as $\phi_{slow} = \phi_{fast} \pm 90°$ and can be obtained for each super-pixel. Note that with using circular light, phase differences of only $\pi/2$ can be measured, due to the range of $\sin^{-1}$ in Eqs. (4.1) and (4.2).

2.4 Determining strain rates from birefringence

From the two-dimensional flow birefringence measurements Δn, we derived the associated strain rates $\dot{\epsilon}$ with the help of reference data. A previous study (Lane, Rode, et al., 2022a) used similar suspensions and reports the birefringence response to shear by using a Taylor–Couette type setup, giving tabulated values $\Delta n(\dot{\gamma})$ for different CNC concentrations. In this study, we make the approximation $\Delta n(\dot{\epsilon}) = \Delta n(\dot{\gamma})$, thus assuming that the birefringence response to any kind of two-dimensional strain rate $\dot{\epsilon}$ (see Eq. (1)) is similar, regardless of it originating from a shearing flow (e.g., $\dot{\epsilon} = |u_y|$), an extensional flow (e.g., $\dot{\epsilon} = |2u_x|$, with $u_x > 0$), or a compressional flow (e.g., $\dot{\epsilon} = |2u_x|$, with $u_x < 0$). We use the inverse mapping of the published data to derive the strain rates (referred to as 'derived strain rates' in the following), hence setting $\dot{\epsilon}(\Delta n) = \dot{\gamma}(\Delta n)$. The reference data were taken using the same wavelength of 600 nm. It is shown in Fig. 4 and serves as a look-up table for determining $\dot{\epsilon}$ from Δn measurements. The measurement technique applied here can only measure birefringence in the range $0 \le \Delta n \le 1.2 \cdot 10^{-5}$ (see Sect. 2.3). Therefore, only the values in that region are of interest to us. Linear interpolation was used between the tabulated values. Note that the Δn resolution of the 1.0 wt% data is higher than that of the 1.2 wt%. This is because the birefringence data were taken at specified shear rates; hence, the $\dot{\epsilon}$ resolutions are the same.

Considering the determination of strain rates from birefringence measurements, the ideal relationship between $\dot{\epsilon} \leftrightarrow \Delta n$ is linear and many birefringence studies measure the strain rates in an operational window where a linear
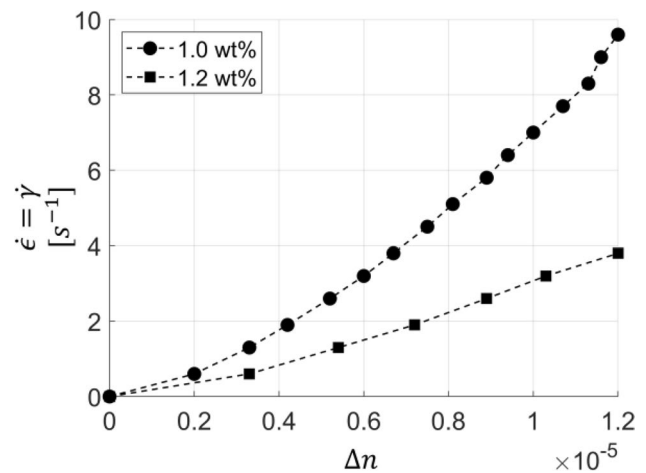

Fig. 4 Reference data $\dot{\epsilon}(\Delta n)$ as published by (Lane, Rode, et al., 2022a). Note that we added the origin (0,0), as the nonzero birefringence values at zero shear rate stated in the paper are thought to result from measurement inaccuracies, which become large at zero birefringence

assumption is reasonable. Generally, however, the relationship is nonlinear and increasing the strain rate increases the birefringence response only up to a point where the degree of particle alignment reaches a maximum and thus, the birefringence response approaches a plateau. At this plateau, an increase in strain rate no longer increases birefringence. This trend can be seen in Fig. 4 by means of a positive second derivative, $d^2\dot{\epsilon}/d\Delta n^2 > 0$, and implies that the accuracy of determining $\dot{\epsilon}$ from birefringence Δn decreases with increasing birefringence. However, we do not consider this to be an issue in this study as Fig. 4 does not show any plateau. Besides this upper limit to the operational window, it is worth mentioning that there is also a lower limit. The onset of hydrodynamic alignment can be described by the Pèclet number $Pe = \dot{\epsilon}/D_r$, where $\dot{\epsilon}$ is the characteristic deformation rate and D_r the rotational diffusion coefficient. For $Pe < 1$, rotational diffusion (Brownian motion) is dominant, whereas for $Pe > 1$ velocity gradients dominate. The present concentrations are thought to be above the dilute regime in the semidilute regime where self-crowding effects must be taken into account and the rotational diffusion coefficient becomes concentration dependent. Calabrese et al. (2022) studied the alignment of colloidal rods in crowded environments and give formulas for calculating the rotational diffusion coefficient. However, applying these or equivalent formulas (Berger Bioucas et al. 2019; Khouri et al. 2014) with our measurement results from Sect. 2.1 lead to an overestimation of the rotational diffusion coefficient. This is thought to result from polydispersity and is explained in the study by Tsvetkov et al. (2017). Birefringence occurs if $Pe > 1$, so a deformation rate of $\dot{\epsilon} \geq D_r$ is necessary to induce birefringence and the rotational diffusion coefficient marks the lower limit the operational window. The smallest nonzero shear rate in Fig. 4 is $0.6\ s^{-1}$, and it is already enough to induce birefringence in both CNC suspensions. As a consequence, the rotational diffusion coefficients for both suspensions are expected to be below this value, $D_r < 0.6 s^{-1}$. For comparison, Tsvetkov et al. (2017) used flow birefringence to determine the rotational diffusion coefficient of CNC particles in water (length and diameter of the majority of CNC particles between 300–600 nm and 25–45 nm, respectively) and obtained $D_r = 0.35 s^{-1}$.

2.5 Fluid flow simulations with Ansys Fluent

Two-dimensional fluid flow simulations of the flow channel depicted in Fig. 3a were performed using the commercial software Ansys Fluent. The CNC suspensions were modeled as Newtonian fluids with an estimated constant viscosity of $10\ mPa \cdot s$ (Shafiei-Sabet et al. 2012). This was done even though it is commonly known that CNC suspensions are non-Newtonian, as they display shear-thinning

(Shafiei-Sabet et al. 2012). However, the suspensions reach a Newtonian plateau for shear rates above $1 \cdot s^{-1}$.

3 Results and discussion

3.1 Plane Poiseuille flow

Figure 5a and b show simulated and derived strain rates, respectively, in the straight channel as well as in the entrance of the constriction. The measurements were done using the 1.2 wt% CNC suspension. The figures are qualitatively and quantitatively similar. Most strain rates are in the range of 0–4 s^{-1} (except in the top right-hand corner of Fig. 5a with values > 4 s^{-1}). Figure 5d compares the measurement results for $x = 18 mm$ to the theoretical solution of a plane Poiseuille flow. A straight channel flow is a shearing flow, and the linear shear rate profile is evident (note that $\dot{\epsilon} = \dot{\gamma} = u_y$ here). In addition, Particle Image Velocimetry (PIV) measurements in the straight channel section showed a parabolic velocity profile. Both findings indicate that a Newtonian assumption is reasonable for the straight channel section. Using the density of water, a viscosity of $10\ mPa \cdot s$, and the hydraulic diameter of the rectangular channel section (8 mm x 25 mm), the estimated Re-number is $Re \approx 3$ and the flow therefore laminar.

The flow studied here is not two-dimensional but in fact three-dimensional. The straight channel section has a rectangular cross section of 8 mm x 25 mm. We use the analytical formulae for the velocity profile of a three-dimensional Poiseuille flow in a rectangular cross section given in Rybiński & Mikielewicz (2014) to study the effect of three-dimensionality. The x–y-z coordinate system used here is shown in Fig. 3a, with the z-axis representing the direction of the optical path. The velocity component in x-direction is u and subscript y indicates the directional derivate. By means of the integral in z-direction, we compare the 3D solution, $u_y(y, z)$, to the 2D solution, $u_{y,2D}(y)$ (plane Poiseuille flow in an 8 mm wide channel). The results are shown in Fig. 5c. We can see that the following relations hold,

$$\int_0^{25mm} u_y(y, z)dz \approx u_{y,2D}(y) \cdot 25mm. \tag{6}$$

This result can be interpreted in the following way: If only the shear rates in the plane perpendicular to the optical path effect birefringence (similar to the concept of secondary principal stresses, which is common in photoelasticity, see Yokoyama et al. (2023) for more information), and if the birefringence response is linear proportional to the shear rate, then the two-dimensional assumption is feasible from an integrated birefringence perspective. However, shear rates
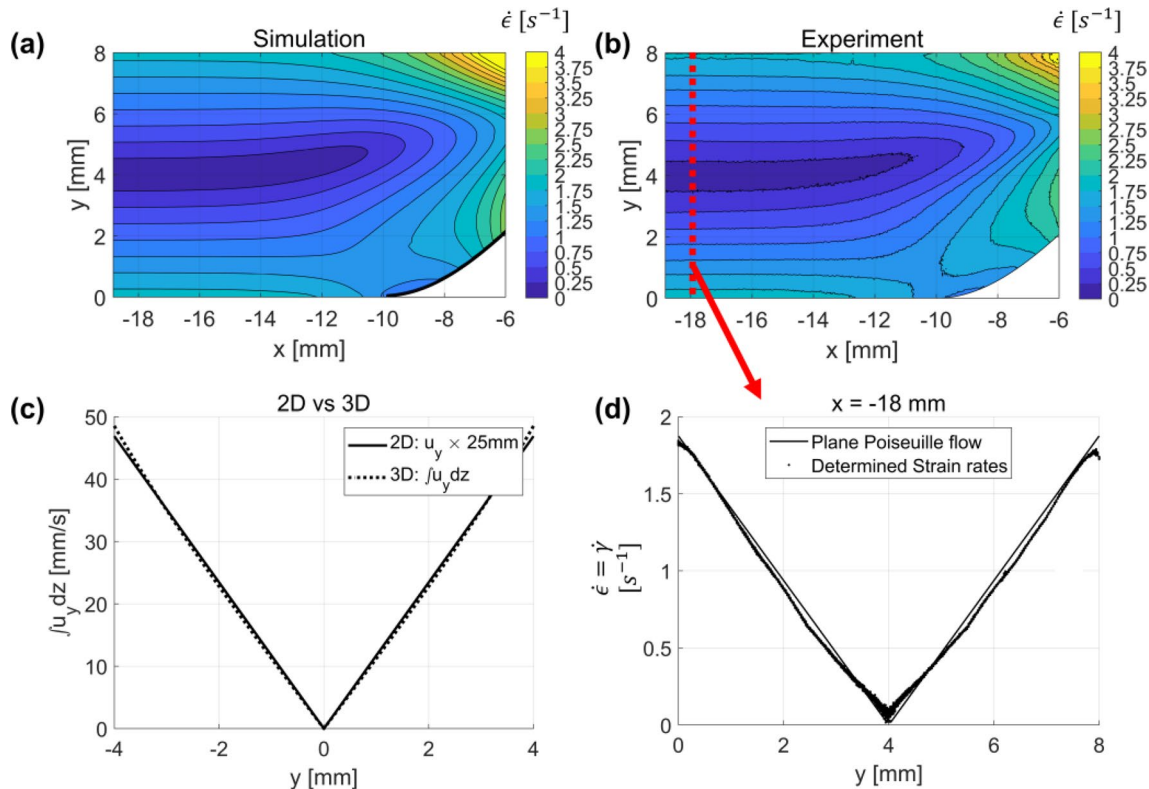
Fig. 5 Plane Poiseuille flow results. Volume flow rate 500 $\mu l/s$ (equivalent to an average flow velocity of 2.5 mm/s). Flow direction from left to right. CNC suspension 1.2 wt%. (**a**) Simulation and (**b**) Experiment results. (**c**) Comparison of integrated shear rates for the 2D and 3D Poiseuille flow. (**d**) Comparison between a plane Poiseuille flow and the derived shear rates for $x = -18mm$

parallel to the optical path can lead to birefringence (see the birefringence response of a plate-plate geometry (Mykhaylyk et al. 2016) as well as the discussion on second-order stress terms in the stress-optic law for three-dimensional flow fields (Nakamine et al. 2023)), and the optical response to shear rate is known to be nonlinear (Lane, Rode, et al. 2022a). Nevertheless, we assume Eq. (6) to be an acceptable approximation. The three-dimensional effect is discussed in a more general approach by Clemeur et al. (2004).

The measurements in the straight channel section show that it is possible to use flow birefringence to derive valid shear rates. The results thus confirm the 1.2 wt% reference data within the investigated range. However, it is important to note that the studied plane Poiseuille flow is similar to the Taylor–Couette flow used in the reference study. The gap width of the referenced Taylor–Couette flow is small compared to the diameter, and thus, the Taylor–Couette flow behaves approximately as a planar Couette flow. Both flow types (plane Poiseuille flow and planar Couette flow) are pure shearing flows with $\dot{\epsilon} = \dot{\gamma} = u_y$, and the material derivatives of the flow velocities $D\vec{u}/Dt$ are zero, meaning that the flows are steady (local derivative $\partial\vec{u}/\partial t = 0$) and the fluid elements do not experience any changes along their streamlines (convective derivative $(\vec{u} \cdot \nabla)\vec{u} = 0$). Therefore,

the present measurements were carried out under similar flow conditions as the reference measurements.

3.2 Flow around the cosine-shaped constriction

Figure 6 shows simulated and derived strain rates for three different flow rates around the cosine-shaped constriction. Strain rates are in the range 0–10 s^{-1}. Reynolds numbers were calculated using the density of water, a viscosity of 10 $mPa \cdot s$, and the hydraulic diameter for the narrowest part of the channel (cross section with 2 mm x 25 mm). This gives estimates of 0.7, 0.9, and 1.2 for flow rates of 100 $\mu l/s$, 125 $\mu l/s$, and 166.6 $\mu l/s$, respectively. Figure 6a, c and e show the simulated strain rates. The contour patterns of the simulations are self-similar and symmetric around the $x = 0mm$ axis. Figure 6b, d, and f show the corresponding experimentally derived strain rates. The contour patterns of the derived strain rates are also self-similar (pattern differences for small strain rates are explained with measurement inaccuracies, as measurement errors are amplified if the birefringence is close to zero (Lane et al. 2021b)). However, the experimentally derived strain rate profiles are unexpectedly asymmetric. The strain rates in the contraction zone in the
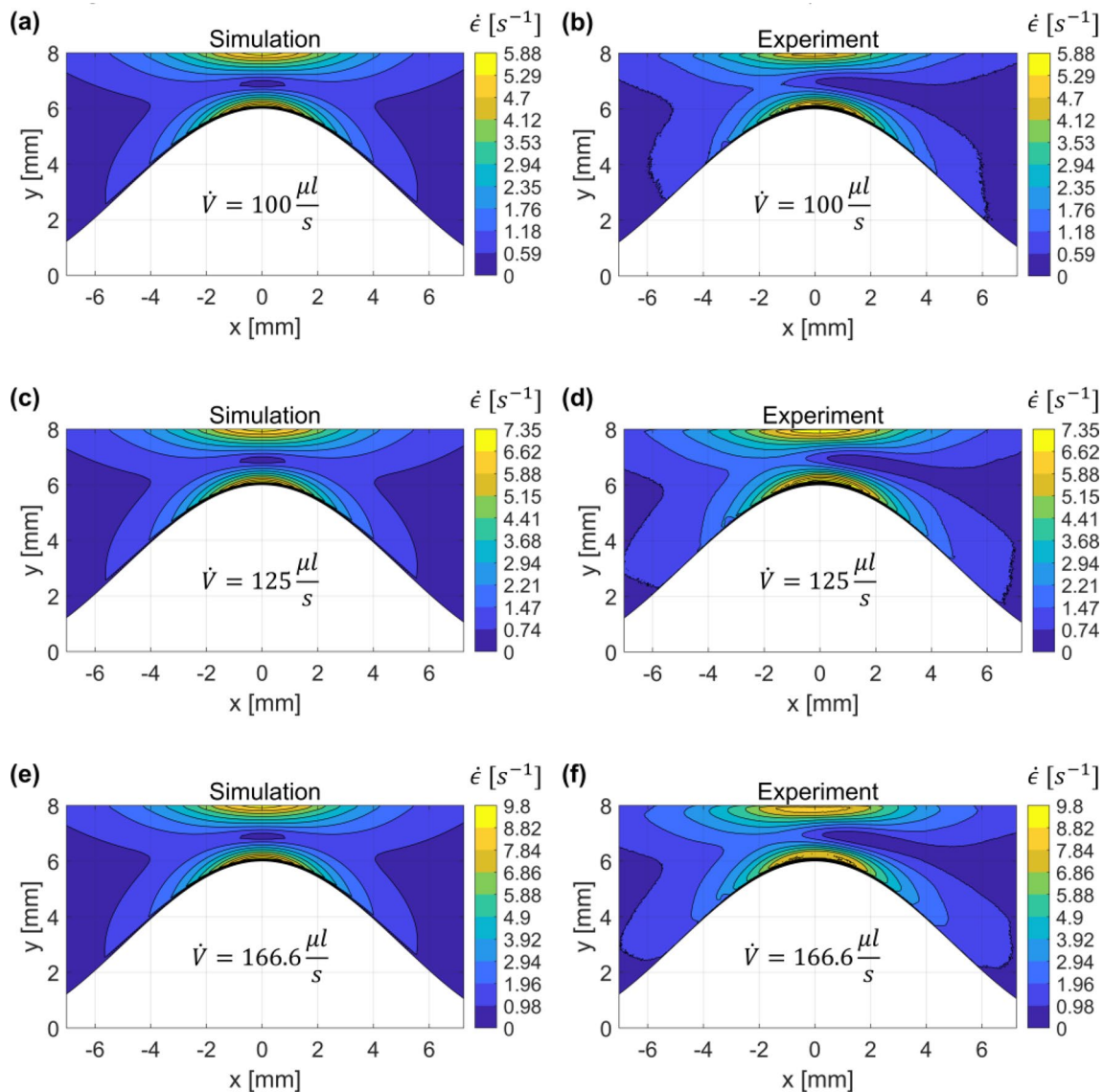
Fig. 6 Simulated vs derived strain rates for flow rates $100\mu l/s$: (**a**) and (**b**), $125\mu l/s$: (**c**) and (**d**), $166.6\mu l/s$: (**e**) and (**f**). Flow direction is from left to right. CNC suspension 1.0 wt%

center of the channel are larger than in the expansion zone. However, close to the walls, the derived strain rates show a similar pattern and are comparable to the simulated strain rates. This fairly good agreement is thought to result from the fact that the flow near the walls is mainly a shear flow.

The direction of the strain rate $\dot{\epsilon}$ can be established by calculating the angle between the positive principal strain rate and the x-axis,

$$\frac{1}{2}\ atan2\left(u_y + v_x, 2u_x\right). \tag{7}$$

The formula can be derived from Mohr's circle and the two-dimensional strain rate tensor. Figure 7a shows the simulated strain rates (same as Fig. 6c) and their corresponding

directions (white lines, calculated using Eq. (7)) for the flow rate of 125 $\mu l/s$. For a pure shearing flow, $\dot{\epsilon} = u_y$, the lines are oriented at 45° toward the flow direction, whereas if only extensional rates are present, $\dot{\epsilon} = \left|2u_x\right|$, the lines are oriented parallel to the flow direction in the contraction zone, $u_x > 0$, and perpendicular to the flow direction in the expansion zone, $u_x < 0$. Applying a circular polarizer and using the technique described in Sect. 2.3, we measure the average direction of the slow refractive index axis, which corresponds to the predominant direction of the longitudinal axis of the nanorods. Figure 7b shows the derived strain rates (same as Fig. 6d) and the measured averaged rod orientations (white lines) for the flow rate of 125 $\mu l/s$. Note that the strain rates were measured using linear polarized light, whereas the rod
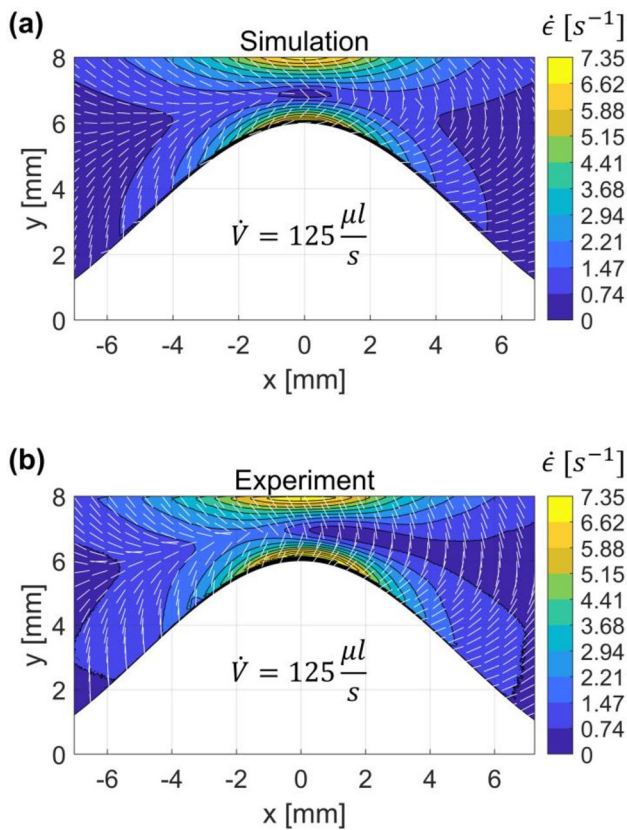
Fig. 7 (**a**) Simulated strain rates and directions of the positive principal strain rate (white lines). (**b**) Derived strain rates (same as Fig. 6d) and measured averaged rod orientations (white lines). Flow direction is from left to right. CNC suspension 1.0 wt%

orientations were measured using circular polarized light. Therefore, Fig. 7b is the result of two measurements. The rods tend to be oriented parallel to the flow in the contraction zone and perpendicular to the flow in the expansion zone.

Before interpreting these findings, we would like to point out one important aspect. As already mentioned in Sect. 3.1, our reference data were obtained in a fluid flow where the material derivative of the flow velocity $D\vec{u}/Dt$ is estimated to be zero. The same is true for the plane Poiseuille flow studied in Sect. 3.1. In both cases, the CNCs within the fluid elements are given enough time to respond to the velocity gradients and these velocity gradients do not change as the associated fluid elements do not experience any flow velocity changes. In the referenced Taylor–Couette experiment, the shear rate was slowly increased and was kept steady for five seconds before recording the images. In Fig. 5, the fluid travelled over $10\,mm$ ($-30\,mm < x < -20\,mm$) at an average flow velocity of $2.5\,mm/s$ before birefringence was measured at $x = -18\,mm$. The fluid flow around the cosine-shaped constriction is different. The flow is steady, but the convective derivative of the flow velocity is generally not zero. Therefore, the fluid elements will experience changing velocity gradients and the CNCs within the fluid elements will need to constantly

adapt. However, this alone does not explain the differences between simulated and experimental results.

We have searched the literature for possible further explanations and found the subsequent studies particularly helpful. Wayland (1960, 1964) defines the angle Λ_0 to be the angle between the direction of the principal strain rate $\dot{\epsilon}$ and the flow direction, giving $\Lambda_0 = 45°$ for a pure shearing flow and $\Lambda_0 \to 0°$ as well as $\Lambda_0 \to 90°$ if the flow is elongated and compressed in the flow direction, respectively. Wayland argues that this angle Λ_0 has an influence on the birefringence response and that Δn is therefore a function of $\dot{\epsilon}$ and Λ_0, leading to $\Delta n = \Delta n(\dot{\epsilon}, \Lambda_0)$. Calabrese et al. (2021) studied the effects of shearing and extensional flows on the alignment of CNCs. For a flow being elongated in the flow direction, the CNCs were oriented in the flow direction, whereas if the flow was compressed in the flow direction, the CNCs were oriented perpendicularly. No distinction is made between positive and negative extensional rates (e.g., elongation and compression) and no difference is reported in their ability to induce particle alignment. The study mentions that extensional rates are 4 times more effective for CNC alignment compared to shear rates. This brings our attention to Eq. (1), because Eq. (1) only accounts for a factor 2 ($\dot{\epsilon} = |2u_x| = |u_y|$). Therefore, the use of a general relationship between strain rate and birefringence response, as described in Sect. 2.4, has to be seen with caution. Trebbin et al. (2013) studied the flow orientation of cylindrical micelles through a narrow microchannel and show that the anisotropic particles align parallel to the flow direction in the contraction zone and perpendicular to the flow direction in the subsequent expansion zone. They argue that the perpendicular alignment is caused by large perpendicular extensional rates resulting from a strong extensional fluid flow and show that the extensional contribution is amplified by shear thinning. The velocity measurements are asymmetric for the contracting and expanding parts of the channel. These differences are explained with the different viscosities parallel and perpendicular to the orientation of the micelles. Our measurements of the main rod orientations depicted in Fig. 7b are consistent with these two studies (Calabrese et al. 2021; Trebbin et al. 2013) and can be explained by the associated extensional rates. Kim et al. (2017) monitored the orientation of rare-earth-doped nanorods for flow shear tomography. They used a birefringence measurement technique to determine the shear rates in a channel with a square-shaped cross section and a semicircular constriction. Similar to our experimental results, the constructed shear rate map is different from the theoretically modeled shear rate map and shows an unexpected asymmetric profile, where the region of maximum shear rate is found in the upstream section and therefore in the contracting part of the constriction. Due to the Reynolds number being small (stated to be about $\sim 10^{-3}$), it is argued that inertia effects are negligible. With the help of computational analysis, the discrepancy between the derived shear

rates and real shear rates is explained as originating from the advection and non-instantaneous reorientation of the nanorods in a non-homogeneous flow. Similar to Kim et al. (2017), we estimate the timescale of advection with $\tau_a = H/U$, where H is the channel width and U the flow velocity. The estimate $D_r < 0.6/s$ from Sect. 2.4 gives $\tau_d = 1/D_r > 1.67s$ for the diffusion timescale. The ratio of the two timescales is the Péclet number, $Pe = \tau_d/\tau_a$, describing the ratio of advection and diffusion. Using the width of the cosine-shaped constriction (2 mm), we get advection timescales of $1s$, $0.8s$, and $0.6s$, leading to $Pe > 1.67$, $Pe > 2.08$, and $Pe > 2.78$ for the flow rates of $100\ \mu l/s$, $125\ \mu l/s$, and $166.6\ \mu l/s$, respectively. Because $Pe > 1$, the orientation of the particles depends not only on the local shear but also on the shear to which the particles have been exposed previously. We therefore explain the asymmetric profiles in Fig. 6b, d, and f and the larger strain rates in the contraction zone as the result of history effects. At this point, it is important to emphasize that flow birefringence is linked to the degree of particle alignment and not directly to local velocity gradients. If the degree of particle alignment is influenced otherwise, e.g., by history effects, the relationship between flow birefringence and local velocity gradients is affected.

4 Conclusion

We have presented a simple method to measure the flow birefringence of aqueous cellulose nanocrystal (CNC) suspensions in a two-dimensional flow. Two types of flows were studied, a plane Poiseuille flow and a flow around a cosine-shaped constriction. Strain rates and averaged particle orientations were derived from birefringence measurements and with the help of reference data. For the plane Poiseuille flow, the derived shear rates agree well with theoretical and computational results. For the flow around the cosine-shaped constriction, the strain rate profile is unexpectedly asymmetric. Based on previous studies, we explain this asymmetric profile to be due to history effects. The CNC particles in the contraction zone tend to align parallel to the flow whereas they tend to align perpendicular to the flow in the expansion zone. These alignments can be explained with dominant extensional rates. Concluding, the study of particle alignment and its influencing factors is of high interest, and the experimental approach and findings of this study appear relevant in this context. The use of flow birefringence to study shear and strain rates is encouraged. However, flow birefringence is linked to the degree of particle alignment and not alone to local velocity gradients. Effects influencing particle alignment must therefore be considered.

Declarations

References

Ajovalasit A, Petrucci G, Scafidi M (2015) Review of RGB photoelasticity. Opt Lasers Eng 68:58–73. https://doi.org/10.1016/j.optlaseng.2014.12.008

Ansys. (2022, January). *Fluent Theory Guide*. https://ansyshelp.ansys.com/account/secured?returnurl=/Views/Secured/corp/v221/en/flu_th/flu_th.html

Berger Bioucas FE, Damm C, Peukert W, Rausch MH, Koller TM, Giraudet C, Fröba AP (2019) Translational and rotational diffusion coefficients of gold nanorods dispersed in mixtures of water and glycerol by polarized dynamic light scattering. J Phys Chem B 123(44):9491–9502. https://doi.org/10.1021/acs.jpcb.9b08274

Bertsch P, Diener M, Adamcik J, Scheuble N, Geue T, Mezzenga R, Fischer P (2018) Adsorption and interfacial layer structure of unmodified nanocrystalline cellulose at air/water interfaces. Langmuir 34(50):15195–15202. https://doi.org/10.1021/acs.langmuir.8b03056

Calabrese V, Haward SJ, Shen AQ (2021) Effects of shearing and extensional flows on the alignment of colloidal rods. Macromolecules 54(9):4176–4185. https://doi.org/10.1021/acs.macromol.0c02155

Calabrese V, Varchanis S, Haward SJ, Shen AQ (2022) Alignment of colloidal rods in crowded environments. Macromolecules 55(13):5610–5620. https://doi.org/10.1021/acs.macromol.2c00769

Clemeur N, Rutgers RPG, Debbaut B (2004) Numerical evaluation of three dimensional effects in planar flow birefringence. J Non-newton Fluid Mech 123(2–3):105–120. https://doi.org/10.1016/j.jnnfm.2004.07.002

Frka-Petesic B, Sugiyama J, Kimura S, Chanzy H, Maret G (2015) Negative diamagnetic anisotropy and birefringence of cellulose nanocrystals. Macromolecules 48(24):8844–8857. https://doi.org/10.1021/acs.macromol.5b02201

Fuller GG (1995) Optical rheometry of complex fluids. Oxford University Press

Hu DL, Goreau TJ, Bush JWM (2009) Flow visualization using tobacco mosaic virus. Exp Fluids 46(3):477–484. https://doi.org/10.1007/s00348-008-0573-6

Jakubek ZJ, Chen M, Couillard M, Leng T, Liu L, Zou S, Baxa U, Clogston JD, Hamad WY, Johnston LJ (2018) Characterization challenges for a cellulose nanocrystal reference material: Dispersion and particle size distributions. J Nanopart Res 20(4):98. https://doi.org/10.1007/s11051-018-4194-6

Janeschitz-Kriegl H (1983). Polymer Melt Rheology and Flow Birefringence. https://doi.org/10.1007/978-3-642-68822-5

Khouri S, Shams M, Tam KC (2014) Determination and prediction of physical properties of cellulose nanocrystals from dynamic light scattering measurements. J Nanopart Res 16(7):2499. https://doi.org/10.1007/s11051-014-2499-7

Kim J, Michelin S, Hilbers M, Martinelli L, Chaudan E, Amselem G, Fradet E, Boilot J-P, Brouwer AM, Baroud CN, Peretti J, Gacoin T (2017) Monitoring the orientation of rare-earth-doped nanorods for flow shear tomography. Nat Nanotechnol 12(9):914–919. https://doi.org/10.1038/nnano.2017.111

Lane C, Rode D, Rösgen T (2021a) Optical characterization method for birefringent fluids using a polarization camera. Opt Lasers Eng 146:106724. https://doi.org/10.1016/j.optlaseng.2021.106724

Lane C, Rode D, Rösgen T (2021b) Two-dimensional birefringence measurement technique using a polarization camera. Appl Opt 60(27):8435. https://doi.org/10.1364/AO.433066

Lane C, Rode D, Rösgen T (2022b) Birefringent properties of aqueous cellulose nanocrystal suspensions. Cellulose. https://doi.org/10.1007/s10570-022-04646-y

Lane C, Rode D, Rösgen T (2022c) Calibration of a polarization image sensor and investigation of influencing factors. Appl Opt 61(6):C37. https://doi.org/10.1364/AO.437391

Lane, C., Baumann, F., & Rösgen, T. (2022). Shear rate imaging using a polarization camera and a birefringent aqueous cellulose nanocrystal suspension. *20th International Symposium on Applications of Laser and Imaging Techniques to Fluid Mechanics, Lisbon, Portugal*.

Lane, C. (2022). *Shear rate imaging using a polarization camera and birefringent aqueous cellulose nanocrystal suspensions* (p. 207 p.) [ETH Zurich; Application/pdf]. https://doi.org/10.3929/ETHZ-B-000574731

Merzkirch W (2001) Streaming Birefringence. Routledge, In Handbook of Flow Visualization

Mitchell B, Yokoyama Y, Nassiri A, Tagawa Y, Korkolis YP, Kinsey BL (2023) An investigation of Hertzian contact in soft materials using photoelastic tomography. J Mech Phys Solids 171:105164. https://doi.org/10.1016/j.jmps.2022.105164

Miyazaki Y, Usawa M, Kawai S, Yee J, Muto M, Tagawa Y (2021) Dynamic mechanical interaction between injection liquid and human tissue simulant induced by needle-free injection of a highly focused microjet. Sci Rep 11(1):14544. https://doi.org/10.1038/s41598-021-94018-6

Mykhaylyk OO, Warren NJ, Parnell AJ, Pfeifer G, Laeuger J (2016) Applications of shear-induced polarized light imaging (SIPLI) technique for mechano-optical rheology of polymers and soft matter materials. J Polym Sci, Part B: Polym Phys 54(21):2151–2170. https://doi.org/10.1002/polb.24111

Nakamine K, Yokoyama Y, Worby W, Muto M, Tagawa Y (2023). *Integrated photoelasticity measurements of a three-dimensional laminar flow: Second-order stress terms in the stress-optic law* [Preprint]. https://doi.org/10.1364/opticaopen.21967049.v1

Onuma T, Otani Y (2014) A development of two-dimensional birefringence distribution measurement system with a sampling rate of 1.3MHz. Optics Communications 315:69–73. https://doi.org/10.1016/j.optcom.2013.10.086

Peebles FN, Liu KC (1965) Photoviscous analysis of two-dimensional laminar flow in an expanding jet: Birefringence patterns are analyzed to determine the velocity distributions in steady, laminar flow. Exp Mech 5(9):299–304. https://doi.org/10.1007/BF02326295

Peebles FN, Prados JW, Honeycutt EH (1964) Birefringent and rheologic properties of milling yellow suspensions. J Polym Sci Part c: Polym Symposia 5(1):37–53. https://doi.org/10.1002/polc.5070050105

Pih H (1980) Birefringent-fluid-flow method in engineering: The development of the two-dimensional birefringent-fluid flow was reviewed. Some results of the application in engineering are given. Recent extension into three-dimensional flows is also discussed. Exp Mech 20(12), 437–444. https://doi.org/10.1007/BF02320884

Rankin GW, Sabbah HN, Stein PD (1989) A streaming birefringence study of the flow at the junction of the aorta and the renal arteries. Exp Fluids 7(2):73–80. https://doi.org/10.1007/BF00207298

Rapet J, Tagawa Y, Ohl CD (2019) Shear-wave generation from cavitation in soft solids. Appl Phys Lett 114(12):123702. https://doi.org/10.1063/1.5083141

Rybiński W, Mikielewicz J (2014) Analytical solutions of heat transfer for laminar flow in rectangular channels. Arch Thermodyn 35(4):29–42. https://doi.org/10.2478/aoter-2014-0031

Schneider, T. (2013). *Spannungsoptik-Tomographie in Strömungen*. https://depositonce.tu-berlin.de/handle/11303/3781

Shafiei-Sabet S, Hamad WY, Hatzikiriakos SG (2012) Rheology of nanocrystalline cellulose aqueous suspensions. Langmuir 28(49):17124–17133. https://doi.org/10.1021/la303380v

Sun C, Huang H-Y (2016) Measurements of flow-induced birefringence in microfluidics. Biomicrofluidics 10(1):011903. https://doi.org/10.1063/1.4939949

Sun Y-D, Sun Y-F, Sun Y, Xu XY, Collins MW (1999) Visualisation of dynamic flow birefringence of cardiovascular models. Opt Laser Technol 31(1):103–112. https://doi.org/10.1016/S0030-3992(99)00023-7

Trebbin M, Steinhauser D, Perlich J, Buffet A, Roth SV, Zimmermann W, Thiele J, Förster S (2013) Anisotropic particles align perpendicular to the flow direction in narrow microchannels. Proc Natl Acad Sci 110(17):6706–6711. https://doi.org/10.1073/pnas.1219340110

Tsvetkov NV, Lebedeva EV, Lezov AA, Perevyazko I, Petrov MP, Mikhailova ME, Lezova AA, Torlopov MA, Krivoshapkin PV (2017) Hydrodynamic and optical characteristics of hydrosols of cellulose nanocrystals. Colloid Polym Sci 295(1):13–24. https://doi.org/10.1007/s00396-016-3975-7

Wayland H (1960) Streaming Birefringence of Rigid Macromolecules in General Two-Dimensional Laminar Flow. J Chem Phys 33(3):769–773. https://doi.org/10.1063/1.1731257

Wayland H (1964) Streaming birefringence as a rheological research tool. J Polym Sci Part c: Polym Symposia 5(1):11–36. https://doi.org/10.1002/polc.5070050104

Yokoyama Y, Mitchell BR, Nassiri A, Kinsey BL, Korkolis YP, Tagawa Y (2023) Integrated photoelasticity in a soft material: Phase retardation, azimuthal angle, and stress-optic coefficient. Opt Lasers Eng 161:107335. https://doi.org/10.1016/j.optlaseng.2022.107335